ACS APPLIED MATERIALS & INTERFACES

www.acsami.org Research Article

Midwavelength Infrared p−n Heterojunction Diodes Based on Intraband Colloidal Quantum Dots

Shihab Bin Hafiz, Mohammad M. Al Mahfuz, Sunghwan Lee, and Dong-Kyun Ko*

Cite This: *ACS Appl. Mater. Interfaces* 2021, 13, 49043−49049 Read Online

ACCESS | Metrics & More | Article Recommendations | Supporting Information

ABSTRACT: As an emerging member of the colloidal semiconductor quantum dot materials family, intraband quantum dots are being extensively studied for thermal infrared sensing applications. High-performance detectors can be realized using a traditional p−n junction device design; however, the heavily doped nature of intraband quantum dots presents a new challenge in realizing diode devices. In this work, we utilize a trait uniquely available in a colloidal quantum dot material system to overcome this challenge: the ability to blend two different types of quantum dots to control the electrical property of the resulting film. We report on the preparation of binary mixture films containing midwavelength infrared Ag_2Se intraband quantum dots and the fabrication of p−n heterojunction diodes with strong rectifying characteristics. The peak specific detectivity at 4.5 μm was measured to be 10^7 Jones at room temperature, which is an orders of magnitude improvement compared to the previous generation of intraband quantum dot detectors.

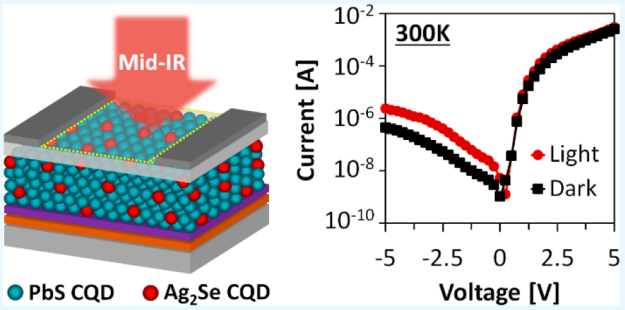

KEYWORDS: *photodiode, intraband, silver selenide, colloidal quantum dots, midwavelength infrared*

INTRODUCTION

The intraband colloidal quantum dots (CQDs) are a new family of semiconductor CQD material that utilizes optical transitions between the first ($1S_e$) and the second ($1P_e$) quantum confined energy levels. The optical gap of $1S_e-1P_e$ can be varied through controlling the CQD size, similar to the traditional interband CQDs, and their absorption peak can span a wide range in the mid- to long-wavelength infrared spectral region.[1−3] The solution processability of these CQDs also allows low-cost, low-temperature, and large-area fabrication of optoelectronic films,[4] which can enable high-throughput manufacturing of infrared imaging focal plane arrays (IRFPAs)[5−7] or construct sensors on a flexible platform.[8] In addition, it has been recently studied that the Auger recombination process can be greatly suppressed in an intraband CQD system,[9,10] and this can potentially lead to high-temperature operation of photodetectors, thereby removing the need for a bulky, high-power-consuming cryogenic cooling system.

Using intraband CQDs, high-performance infrared sensing devices can be fabricated by forming a p−n junction—a traditional diode device design where a built-in electric field established at the junction assists in photoexcited carrier separation and collection.[11−13] The primary advantage of utilizing a p−n diode design lies in the fact that, under a typical reverse-biased operation, the dark current is fed by the minority carriers.[14] Compared to photoconductive[15,3] and barrier device[16,17] designs, where the majority carriers are responsible for the dark current, the p−n junction diode is hence expected to show significant reductions in the magnitudes of the dark current and noise current density. However, the intraband CQDs also present a new and unique challenge when they are used to construct p−n junction devices. To achieve maximum photocarrier collection efficiency, the photodiode is designed such that the depletion region is formed predominantly toward the infrared absorber film, where the photoexcited carriers are created upon illumination. The basic semiconductor physics tells us that the width of this depletion region is inversely proportional to the film's carrier concentration.[14] However, since the first conduction energy level ($1S_e$) is occupied with electrons in intraband CQDs, the film exhibits a high electron carrier concentration (degenerately n-doped), thereby greatly reducing the depletion width formed inside the intraband CQD film. Also, from an electrical point of view, the device will consist of p^+ (heavily doped p-type layer to induce the formation of a depletion region toward the opposite n-type layer) and n^+

Received: August 3, 2021
Accepted: September 22, 2021
Published: October 6, 2021

https://doi.org/10.1021/acsami.1c14749
ACS Appl. Mater. Interfaces 2021, 13, 49043−49049

(degenerately doped n-type intraband CQD layer) materials, which will rather form a tunnel diode (Esaki diode)[18] that will exhibit high reverse-biased tunneling current, with a weak rectifying characteristic.

In this work, we utilize a trait uniquely available in the colloidal quantum dot material system to overcome this challenge. We take advantage of the ability to easily blend two different types of CQDs to control the electrical property of the resulting film. Specifically, we form a mixture of midwavelength infrared (MWIR)-absorbing intraband Ag_2Se CQDs and interband PbS CQDs that act to block the transport of ground state electrons and holes while providing an unimpeded flow of photoexcited electrons, as depicted in Figure 1. Using this binary CQD approach, the number of free

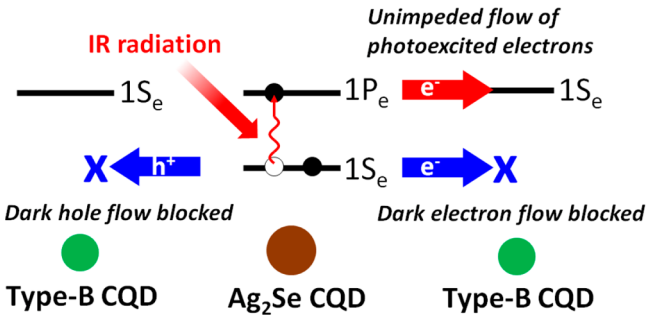

Figure 1. Schematic depicting the mechanism whereby creating a binary CQD mixture leads to an increase in dark resistivity, while the flow of photoexcited electrons is unimpeded.

carriers is greatly reduced (ground state electrons and holes become immobile), which is evidenced by the orders of magnitude increase in the dark resistivity (binary CQD film: 2×10^5 Ω·cm vs Ag_2Se CQD-only film: 1×10^3 Ω·cm, see Supporting Information S1). Also, in junction with ZnO nanoparticle film, which is a layer commonly used to form p−n junctions with PbS CQDs in many CQD solar cell studies,[19] this binary CQD film will exhibit strong rectifying $I-V$ characteristics. It is worth noting that the unique binary CQD approach presented here can be modified to allow/block the flow of dark/photocarriers by changing the CQD size or employing different types of CQDs.[20]

RESULTS AND DISCUSSION

Based on our previous study on the energy level alignment between Ag_2Se and PbS CQDs,[16,17] a Ag_2Se CQD with an average size of 5.5 nm and a PbS CQD with an average size of 3 nm should create a binary CQD system with decreased dark free carriers (Figure 1). First, to prepare the CQD materials, Ag_2Se and PbS CQDs were synthesized following previously reported hot-injection protocols.[16] Figure 2a shows the mid-infrared optical absorption of films made from as-synthesized Ag_2Se, PbS, and mixed (optimized mixture ratio of N_{Ag2Se}/N_{PbS} = 0.04, see more details in Figure 4b) CQDs obtained using Fourier transform infrared (FTIR) spectroscopy. The PbS CQDs capped with oleic acid show an absence of absorption in a 3.5−6 μm spectral range, which makes them a good candidate for use in the binary CQD approach to modify the film's electrical property. The characteristic peaks around 3.4 μm arise due to vibrational modes of C−H, and the peaks around 4.4, 6.5, and 7.2 μm originate from CO_2. Another peak at 7.8 μm (1285 cm^{-1}) arises from the C−O stretch of the

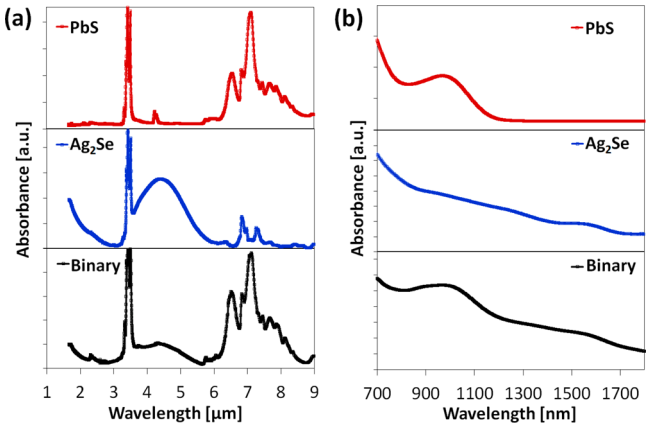

Figure 2. Optical absorbance characterization of as-synthesized PbS, Ag_2Se, and PbS/Ag_2Se mixture CQDs using (a) Fourier transform infrared (FTIR) and (b) visible−near-infrared spectroscopies.

oleic acid ligand. The Ag_2Se CQD film shows a distinct intraband absorption peak centered at 4.2 μm, which optically resides within the transparent window of PbS CQDs. Peaks shown around 6.8 μm arise from vibrational modes of trioctylphosphine (TOP). The film composed of a binary PbS/Ag_2Se CQD mixture shows the sum of PbS and Ag_2Se absorption, where the MWIR absorption peak at 4.2 μm arising from Ag_2Se CQD is still predominant. Figure 2b shows optical spectra in the visible to near-infrared spectral region obtained from the same CQDs. The PbS CQD shows an absorption peak at 1000 nm, which is in agreement with the CQD size of 3 nm.[21] On the other hand, Ag_2Se CQDs show a continuous increase in absorbance (without any visible absorption peaks) with decreasing wavelength as the density of states and the number of available transition pathways increase with increasing energy. The binary CQD mixture sample shows a spectrum that combines the optical absorption arising from Ag_2Se and PbS CQDs.

To fabricate the device, a Cr/Au electrode is first prepatterned on a glass substrate using a shadow mask to form a bottom contact. Then, a thin layer of MoO_x (15 nm) is deposited by thermal evaporation. MoO_x has been frequently used in PbS CQD solar cell devices to improve contact between PbS CQD and the metal electrode.[22,23] We adopt this approach in our devices, since our binary CQD layer is majorly composed of PbS CQDs, in which Ag_2Se CQDs are embedded sparsely as MWIR absorbers or sensitizers. Next, a binary PbS/Ag_2Se CQD layer was deposited using spin-casting and a ligand-exchange procedure using 1,2-ethanedithiol (EDT) was carried out to improve the electronic coupling between CQDs.[24] The thickness of the binary CQD layer was increased by repeating this step 10−12 times to create a 200 nm-thick film. It is worth noting that ligand-exchange duration is not a critical processing parameter for binary CQD devices. Devices fabricated from pure Ag_2Se CQDs, in contrast, showed a narrow temporal window that exhibits the maximum MWIR responsivity.[16] This can be understood by reflecting the fact that the majority component of our binary CQD film is PbS CQDs. To form a p−n junction, ZnO nanoparticles were synthesized following the literature report[25,26] and spin-casted on top of a binary CQD layer with a thickness of 80 nm (see the Supporting Information S2 for optical absorption of ZnO in the mid-infrared). To complete the device, an Al top contact having two finger electrodes was deposited through a shadow

https://doi.org/10.1021/acsami.1c14749
ACS Appl. Mater. Interfaces 2021, 13, 49043−49049

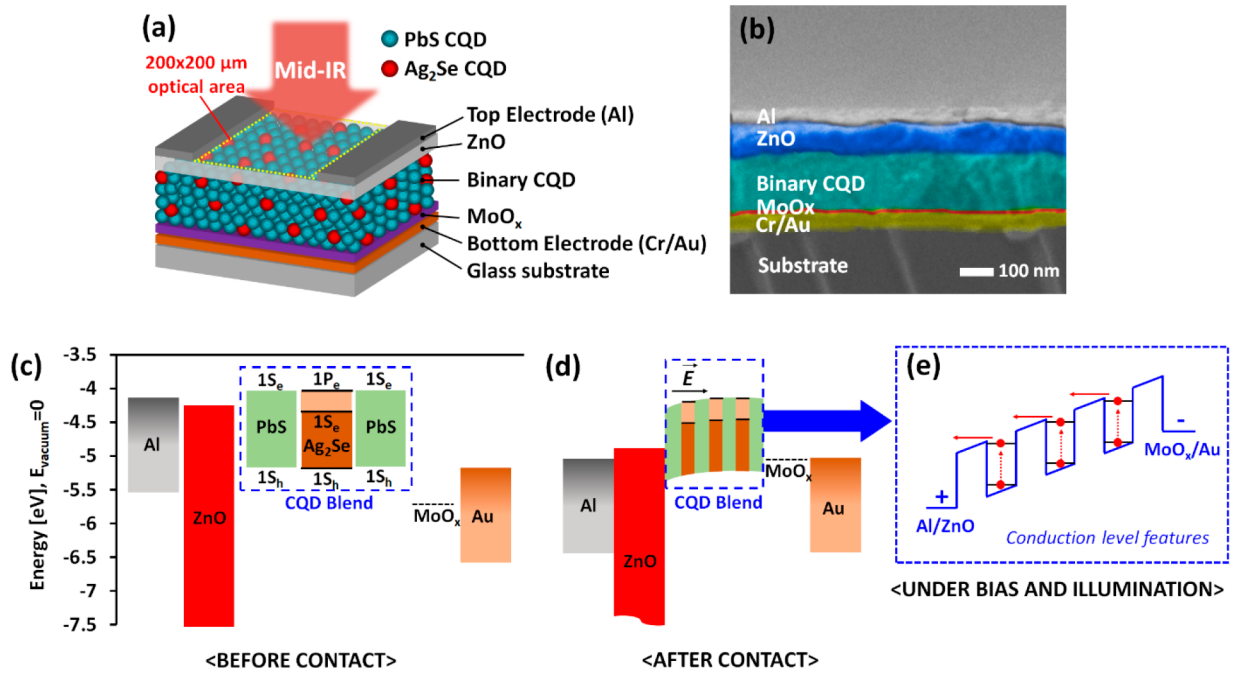

Figure 3. Fabrication of p−n junction diode using binary CQD. (a) Schematic illustration of the device structure, which consists of a glass substrate, bottom contact (Cr/Au), MoO_x layer, PbS/Ag_2Se CQD mixture layers, ZnO nanoparticle layer, and top contact (Al). (b) shows a false-color cross-sectional SEM image of the fabricated device. (c) shows the energy level alignment before contact. $1S_h$, $1S_e$, and $1P_e$ denote first valence energy level, first conduction energy level, and second conduction energy level, respectively. (d) shows the equilibrium energy level diagram after contact. $\vec{E}$ denotes the built-in electric field. (e) depicts the conduction level features of the binary CQD system under bias and with infrared illumination.

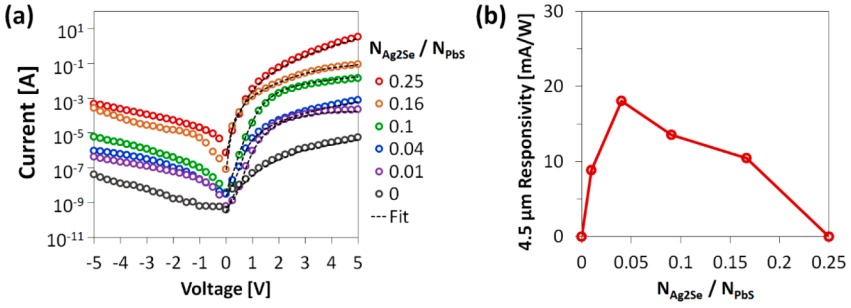

Figure 4. Electrical characterization of binary CQD p−n junction diodes. (a) A series of dark I−V characteristics obtained from diodes with different binary CQD mixing ratios. The open symbols are experimental data, while the dashed lines are the fittings based on the diode equation. (b) Responsivity at 4.5 μm plotted as a function of the binary CQD mixing ratio.

mask (see the Supporting Information S3 for Ohmic contact formation). The top opening created by the fingers defines our device's optical area of 200 × 200 μm. A schematic illustration of this upward-looking photodiode is shown in Figure 3a, and the cross-sectional scanning electron microscope (SEM) image of the device is shown in Figure 3b. Figure 3c shows the energy level alignment of our binary CQD p−n junction device materials before contact. After contact, a ZnO−PbS CQD n−p junction[27] will establish a built-in electric field ($\vec{E}$) toward the binary CQD layer where the Ag_2Se CQDs reside (Figure 3d). Under bias and with infrared illumination, photoexcited electrons generated from the Ag_2Se CQDs will cascade down toward the Al cathode, bearing a resemblance to the operation of epitaxial quantum dot infrared photodetectors (QDIPs)[28,29] as illustrated in Figure 3e.

Prior to the photodetector performance characterizations, we carried out basic electrical measurements of our p−n junction diode devices, under dark, with a varying binary CQD mixture ratio. The ratio of N_{Ag2Se}/N_{PbS} = 0.25, for example, denotes a CQD film having 25 Ag_2Se CQDs per 100 PbS CQDs (see Supporting Information S4 for details). A series of current−voltage (I−V) characteristics were obtained (Figure 4a) and were fitted to a standard diode equation[30]

$$I = I_o\left\{\exp\left[\frac{q}{nkT}(V - IR_s)\right] - 1\right\} + \frac{V - IR_s}{R_{sh}} \quad (1)$$

where n is the ideality factor, I_o is the dark saturation current, R_s is the series resistance, and R_{sh} is the shunt resistance. We extract four key diode parameters as summarized in Table 1. First, we observe that all diodes exhibit an ideality factor (n) larger than 3. While n typically varies between 1 and 2, $n > 3$ is also frequently reported in diodes with nonideal electrical contacts.[31−33] This indicates an existence of a contact barrier formed at either the Al/ZnO or binary CQD/MoO_x−Au interface in our devices. The value of n showing irrelevance to

https://doi.org/10.1021/acsami.1c14749
ACS Appl. Mater. Interfaces 2021, 13, 49043−49049

Table 1. Summary of Diode Parameters Extracted from *I*−*V* Characteristics

N_{Ag2Se}/N_{PbS}	ideality factor (n)	saturation current I_o (A)	shunt resistance R_{sh} (Ω)	series resistance R_s (Ω)
0	3.2	3.0×10^{-10}	1.7×10^{5}	4.7×10^{2}
0.01	3.8	5.0×10^{-8}	7.6×10^{4}	2.6×10^{2}
0.04	3.2	5.2×10^{-8}	2.7×10^{3}	0.9×10^{2}
0.1	3.7	9.5×10^{-8}	2.2×10^{3}	1.6×10^{2}
0.16	3.4	4.0×10^{-6}	1.5×10^{3}	0.4×10^{2}
0.25	3.8	8.0×10^{-6}	0.9×10^{3}	0.5×10^{2}

the N_{Ag2Se}/N_{PbS} ratios points to a fact that a barrier may be formed at the Al/ZnO interface. On the other hand, for the reverse saturation current I_0, we observe a distinct trend where increasing Ag_2Se CQD loading (increasing N_{Ag2Se}/N_{PbS} ratio) dramatically increases the magnitude of I_0. The value I_0 is indicative of how much recombination there is in the p−n junction device.[34,35] This suggests that as we increase the number of Ag_2Se CQDs in the binary CQD film, Ag_2Se CQD itself or the surface defects associated with Ag_2Se CQD increases the rate of carrier recombination inside the device. This, in turn, influences the optimum binary CQD mixture ratio that yields the highest MWIR peak responsivity in our diode devices, as shown in Figure 4b. Figure 5b shows the 4.5

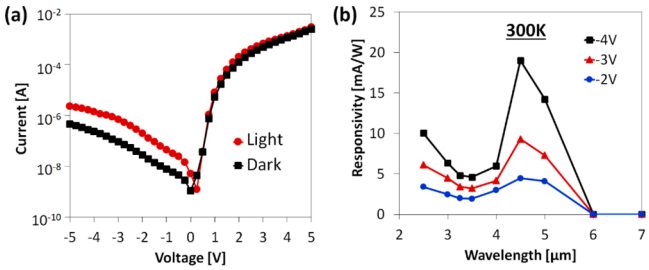

Figure 5. Detector performance characterization of binary CQD diode devices with an optimized CQD mixture ratio. (a) shows the *I*−*V* characteristics of the device under dark and under infrared illumination. The illumination was provided by a 900 °C calibrated blackbody with a Ge filter. (b) shows the spectral responsivity measured at various bias voltages. All devices were measured at room temperature, 300 K.

μm peak responsivity of our diode device as a function of the N_{Ag2Se}/N_{PbS} ratio. At $N_{Ag2Se}:N_{PbS} = 0$, the absence of MWIR-absorbing Ag_2Se CQD induces zero photocurrent at 4.5 μm. As we increase the Ag_2Se CQD loading, the peak responsivity increases, because more Ag_2Se CQDs will produce a larger number of photoexcited carriers upon infrared illumination. However, as we increase the Ag_2Se CQD loading further, the increase in the photocarrier generation will compete with the increase in the carrier recombination. It is observed that for $N_{Ag2Se}/N_{PbS} > 0.04$, the peak responsivity starts to decrease, suggesting that the carrier recombination arising from Ag_2Se CQDs starts to overweight the optical generation. Hence, we observe a peak at $N_{Ag2Se}/N_{PbS} = 0.04$, which we define as the optimum binary CQD mixture ratio for MWIR detection. Another important diode parameter of a p−n junction is the shunt resistance R_{sh}, which arises from the presence of an electrical shunt path (current leakage) through the p−n junction.[36] In our devices, high R_{sh} is observed for pure CQD film ($N_{Ag2Se}/N_{PbS} = 0$), and R_{sh} decreases with increasing Ag_2Se CQD loading. This can be understood by reflecting the fact that, in our binary CQD system, as more Ag_2Se CQDs are introduced, the probability of Ag_2Se CQDs creating a direct percolation path (a highly conductive path, since Ag_2Se CQDs are degenerately n-doped) is more frequent inside the film. This is illustrated in the Supporting Information S5. Lastly, the series resistance R_s is indicative of additional series resistance components present in the device, typically arising from high contact resistances.[34] For R_s, we do not observe any particular trend with Ag_2Se CQD loading, and all the devices show a magnitude of R_s around 10^2 Ω.

Using a diode device with the optimum binary CQD mixing ratio identified in Figure 4b ($N_{Ag2Se}/N_{PbS} = 0.04$), we characterized the detector performance parameters using the infrared illumination provided by a calibrated blackbody heated at 900 °C, filtered through Ge, which cuts off photons with a wavelength smaller than 1.8 μm. Figure 5a shows the diode *I*−*V* characteristics obtained under dark and under infrared illumination conditions. The dark *I*−*V* shows strong rectifying characteristics with an on/off ratio of 6×10^3 at ±5 V. Upon illumination, the device showed a distinct increase in a reverse-biased current with a photovoltage of 250 mV. Figure 5b shows the spectral responsivity of the device collected at room temperature by replacing the Ge filter with a set of band-pass filters with center wavelengths varying from 2.5−7 μm and measuring the photocurrent using a lock-in technique. The magnitude of photocurrent (~0.17 μA) estimated from the difference between the dark and light curve at a reverse bias of −2.0 V, closely matches with the photocurrent (~0.20 μA) calculated by integrating the area under the curve of spectral photocurrent data extracted from responsivity spectra at a corresponding bias of −2.0 V. The peak responsivity is obtained at 4.5 μm with the magnitude of the responsivity increasing with increasing reverse bias and reaches a value of 19 mA/W at −4 V. This 4.5 μm peak coincide with the optical absorption arising from Ag_2Se CQDs along with the shape of the spectrum (Figure 2a), indicating that the device responsivity primarily arises from Ag_2Se CQDs inside the binary CQD film. The noise current density (i_n) measured using our spectrum analyzer in 1 Hz bandwidth was 4.91×10^{-11} A $Hz^{-1/2}$ (see Supporting Information S7 for more details). Using these values, specific detectivity ($D^* = \frac{RA^{1/2}}{i_n}$, where A is the detector area, i_n is the noise current density, and R is the responsivity) is calculated to be 7.8×10^6 Jones at 300 K (see Supporting Information S8). This is a 30 times increase over our previous generation of barrier devices.[16] This improvement is mainly attributed to the reduced dark current and noise current density, an advantageous device property offered by reverse-biased p−n junction diodes.

CONCLUSIONS

In summary, we have demonstrated intraband CQD-based photodiodes exhibiting a strong rectifying characteristic and reduced dark current and noise current density, with MWIR detectivity reaching 7.8×10^6 Jones without cooling. This was enabled by our binary CQD approach, which helped to overcome the issue arising from the degenerately doped nature of intraband Ag_2Se CQDs.

In our binary CQD devices, we defined $N_{Ag2Se}/N_{PbS} = 0.04$ as the optimum mixture ratio for MWIR detection, as discussed in relation to Figure 4b data. It is anticipated that this ratio could increase, thereby improving the MWIR

https://doi.org/10.1021/acsami.1c14749
ACS Appl. Mater. Interfaces 2021, 13, 49043−49049

responsivity, if the surface passivation of CQDs can be enhanced. Further improvements in the device performance are anticipated through optimizing the contact properties and investigating various surface capping ligands that can enhance the carrier mobilities in conjunction with improving the surface passivation.[37−40]

METHODS

Chemicals. Oleylamine (OLA, 70%), trioctylphosphine (TOP, 90%), selenium (Se, 99.999%), silver chloride (AgCl, 99%), lead oxide (PbO, 99.999%), hexamethyldisilathiane (TMS_2S, synthesis grade), 1-octadecene (ODE, 90%), oleic acid (OA, 90%), potassium hydroxide (KOH, 85%), zinc acetate dihydrate ($Zn(CH_3COO)_2{\cdot}2H_2O$, 98%), 1,2-ethanedithiol (EDT, 98.0%), 1-butanol (99.8%), hexane (98.5%), methanol (99.8%), octane (99%), chloroform (99.8%), and ethyl alcohol (99.5%) were purchased from Sigma-Aldrich and were used as received.

Ag_2Se CQD Synthesis. Ag_2Se CQDs with an absorption peak at 4.2 μm were synthesized following the previously reported procedure.[41,16] At first, 1 M selenium precursor solution was prepared by dissolving Se powder in trioctylphosphine (TOP−Se), and 0.5 M silver precursor solution was prepared by dissolving AgCl in trioctylphosphine (TOP−Ag) inside glovebox. Then, 30 mL of oleylamine was heated to 90 °C under vacuum in a three-neck flask. After degassing the solution for 1 h, the atmosphere was switched to nitrogen. Then, 8 mL of 1 M TOP−Se was injected at the temperature of 130 °C. To increase the synthetic yield, 800 μL of diphenylphosphine was added to 16 mL of 0.5 M TOP−Ag. The solution was rapidly injected, and the reaction continued for 20 s. Then, 20 mL of butanol was injected into the reaction mixture, followed by cooling in a water bath to room temperature. The CQDs were precipitated with a mixture of ethanol and methanol by centrifugation. The resulting CQDs were washed three times with methanol and redispersed in octane (see Supporting Information S9).

PbS CQD Synthesis. PbS CQDs with an absorption peak at 1000 nm were synthesized following a previously developed protocol.[42,43] In this procedure, 0.45 g of lead oxide was dissolved in 10 mL of 1-octadecene and 2 mL of oleic acid, and the solution was heated to 110 °C in a three-neck flask under vacuum for 1 h. Then, 0.2 mL of hexamethyldisilathiane was added to 5 mL of anhydrous 1-octadecene to prepare the sulfur precursor solution, which was injected rapidly at 110 °C under nitrogen environment into the reaction flask. The color of the solution turned dark brown immediately after the injection, and the solution was cooled naturally. After the synthesis, the CQDs were precipitated using acetone by centrifugation inside the glovebox and the final QDs were redispersed in a mixture of hexane and octane.

ZnO Nanoparticle Synthesis. ZnO nanoparticles were synthesized by following the literature method.[25,26] In this procedure, 1.4 g of zinc acetate dihydrate ($Zn(CH_3COO)_2{\cdot}2H_2O$) was dissolved in 60 mL of methanol, and the solution was transferred to a three-neck flask at 65 °C. Then, 0.70 g of potassium hydroxide (KOH) was dissolved in 30 mL of methanol, and the solution was added dropwise to the zinc acetate solution for about 5 min with constant stirring. A milky white solution was obtained after stirring the mixture for 2 h 30 min at 65 °C. The mixture was naturally cooled for 1 h. Finally, the ZnO nanoparticles were precipitated by centrifugation and dissolved in 5 mL of chloroform to prepare an optically transparent solution.

Device Fabrication. Glass substrates (10 × 10 mm) were used to fabricate p−n junction devices. First, the substrate was sonicated with isopropyl alcohol, acetone, and hexane, flushed with isopropyl alcohol and dried with N_2 gas flow. A bottom contact of 50 nm (Cr/Au) was then deposited using a shadow mask by thermal evaporation. Next, 20 nm MoO_x was blanket deposited using thermal evaporation. Both bottom contact (Cr/Au) and MoO_x were deposited at a rate of 1 Å/s under a vacuum of 2×10^{-6} mbar. For preparing the binary CQD solution, Ag_2Se and PbS QD solution were mixed in a glass vial and stirred with vortex machine for 60 s and filtered through a 0.2 μm PTFE syringe filter prior to deposition. A total of 10−12 layers of CQD blend solution were deposited via spin coating at 2000 rpm for 30 s. After each layer of the CQD film deposition, the device was ligand-exchanged by dipping it in 0.01 M 1,2-ethanedithiol (in methanol) for 30 s and rinsing it with methanol for 20 s. On top of binary CQD layers, two layers of ZnO were deposited by spin coating (2500 rpm, 30 s). For top contact, 50 nm aluminum with an optical opening of 200 × 200 μm defined by two finger electrodes was deposited by thermal evaporation through a shadow mask.

Characterization. For optical absorption characterization, Fourier transform infrared (FTIR) spectra were collected using a Thermo Nicolet 370 FTIR spectrometer. Absorption spectra in the visible to near-infrared range were collected using StellarNet UV−vis−NIR spectrometer (RW-NIRX-SR and BLK-CXR). A scanning electron microscopy (SEM) cross-sectional image of the device was collected by JEOL JSM-7900F.

For electrical characterization, current−voltage measurements were performed by a semiconductor parameter analyzer (Agilent 4155). For photocurrent measurements, a calibrated blackbody (Newport 67030, 900 °C) was used as the infrared illumination source. A germanium (Ge) long-pass filter was used to cut off short-wavelength infrared photons. For the spectral photocurrent, a set of Fabry−Perot band-pass filters was used, having center wavelengths varying from 2.5 to 7 μm. This illumination source was chopped at 15 Hz using an optical chopper. The photocurrent was measured by a lock-in amplifier (SR830) coupled with a preamplifier (SR570), where the preamplifier provided the required bias. The responsivity was determined by dividing the measured photocurrent with the optical illumination power calculated for each filter. To determine the specific detectivity of the device, the noise current density was measured at 15 Hz with a spectrum analyzer (SR760), where a preamplifier (SR570) was used to provide low-noise bias to the device. The spectrum analyzer, preamplifier, and the device were kept inside a Faraday cage and were grounded to minimize external noise. The specific detectivity was determined using the measured responsivity and noise current density values.

ASSOCIATED CONTENT

Supporting Information

The Supporting Information is available free of charge at https://pubs.acs.org/doi/10.1021/acsami.1c14749.

I−*V* characteristics of Ag_2Se, PbS, and binary CQD devices, FTIR spectrum of ZnO nanoparticle film, Ohmic contact characteristics, binary CQD mixing ratio equation, evolution of shunt current path, photocurrent vs time plot, noise current density vs frequency plot, table summarizing performance parameters, TEM image of Ag_2Se CQDs (PDF)

AUTHOR INFORMATION

Corresponding Author

Dong-Kyun Ko − *Department of Electrical and Computer Engineering, New Jersey Institute of Technology, Newark, New Jersey 07102, United States;* orcid.org/0000-0003-1834-0241; Email: dkko@njit.edu

Authors

Shihab Bin Hafiz − *Department of Electrical and Computer Engineering, New Jersey Institute of Technology, Newark, New Jersey 07102, United States*

Mohammad M. Al Mahfuz − *Department of Electrical and Computer Engineering, New Jersey Institute of Technology, Newark, New Jersey 07102, United States*

Sunghwan Lee − *School of Engineering Technology, Purdue University, West Lafayette, Indiana 47907, United States;* orcid.org/0000-0001-6688-8995

Complete contact information is available at:

https://pubs.acs.org/10.1021/acsami.1c14749

Notes

The authors declare no competing financial interest.

■ ACKNOWLEDGMENTS

This work was supported by the US National Science Foundation under Grant ECCS-1809112.

■ REFERENCES

(1) Shen, G.; Chen, M.; Guyot-Sionnest, P. Synthesis of Non-aggregating HgTe Colloidal Quantum Dots and the Emergence of Air-Stable n-Doping. *J. Phys. Chem. Lett.* **2017**, *8*, 2224−2228.
(2) Lhuillier, E.; Scarafagio, M.; Hease, P.; Nadal, B.; Aubin, H.; Xu, X. Z.; Lequeux, N.; Patriarche, G.; Ithurria, S.; Dubertret, B. Infrared Photodetection Based on Colloidal Quantum-Dot Films with High Mobility and Optical Absorption up to THz. *Nano Lett.* **2016**, *16*, 1282−1286.
(3) Hafiz, S. B.; Scimeca, M.; Sahu, A.; Ko, D.-K. Mid-Infrared Colloidal Quantum Dot Based Nanoelectronics and Nano-Optoelectronics. *ECS Trans.* **2019**, *92*, 11−16.
(4) Kagan, C. R.; Lifshitz, E.; Sargent, E. H.; Talapin, D. V. Building Devices from Colloidal Quantum Dots. *Science* **2016**, *353*, aac5523.
(5) Buurma, C.; Pimpinella, R. E.; Ciani, A. J.; Feldman, J. S.; Grein, C. H.; Guyot-Sionnest, P. MWIR Imaging with Low Cost Colloidal Quantum Dot films. *Proc. SPIE* **2016**, *9933*, 993303.
(6) Chatterjee, A.; Pendyala, N. B.; Jagtap, A.; Rao, K. S. R. K. Uncooled Mid-Wave Infrared Focal Plane Array using Band Gap Engineered Mercury Cadmium Telluride Quantum Dot Coated Silicon Roic. *e-J. Surf. Sci. Nanotechnol.* **2019**, *17*, 95−100.
(7) Qiu, J.; Weng, B.; McDowell, L. L.; Shi, Z. Low-Cost Uncooled MWIR PbSe Quantum Dots Photodiodes. *RSC Adv.* **2019**, *9*, 42516−42523.
(8) Tang, X.; Ackerman, M. M.; Guyot-Sionnest, P. Flexible Infrared Electronic Eyes for Multispectral Imaging with Colloidal Quantum Dots. *International Conference on Optical Instruments and Technology: IRMMW-THz Technologies and Applications* **2019**, *11441*, 114410E.
(9) Melnychuk, C.; Guyot-Sionnest, P. Multicarrier Dynamics in Quantum Dots. *Chem. Rev.* **2021**, *121*, 2325−2372.
(10) Melnychuk, C.; Guyot-Sionnest, P. Auger Suppression in n-Type HgSe Colloidal Quantum Dots. *ACS Nano* **2019**, *13*, 10512−10519.
(11) Hafiz, S. B.; Scimeca, M. R.; Sahu, A.; Ko, D.-K. Colloidal Quantum Dots for Thermal Infrared Sensing and Imaging. *Nano Convergence* **2019**, *6*, 7.
(12) Chen, H.; Liu, H.; Zhang, Z.; Hu, K.; Fang, X. Nanostructured Photodetectors: From Ultraviolet to Terahertz. *Adv. Mater.* **2016**, *28*, 403−433.
(13) Chen, J.; Ouyang, W.; Yang, W.; He, J.-H.; Fang, X. Recent Progress of Heterojunction Ultraviolet Photodetectors: Materials, Integrations, and Applications. *Adv. Funct. Mater.* **2020**, *30*, 1909909.
(14) Streetman, B.; Banerjee, S. *Solid State Electronic Devices*, 7th ed.; Pearson, 2014.
(15) Hafiz, S. B.; Scimeca, M. R.; Zhao, P.; Paredes, I. J.; Sahu, A.; Ko, D.-K. Silver Selenide Colloidal Quantum Dots for Mid-Wavelength Infrared Photodetection. *ACS Appl. Nano Mater.* **2019**, *2*, 1631−1636.
(16) Hafiz, S. B.; Al Mahfuz, M. M.; Ko, D.-K. Vertically Stacked Intraband Quantum Dot Devices for Mid-Wavelength Infrared Photodetection. *ACS Appl. Mater. Interfaces* **2021**, *13*, 937−943.
(17) Hafiz, S. B.; Al Mahfuz, M. M.; Ko, D.-K. Intraband Quantum Dot Barrier Devices - Optimization of Energy Level Alignment. *ECS Trans.* **2021**, *102*, 45−51.
(18) Sze, S. M.; Ng, K. K. *Physics of Semiconductor Devices*, 3rd ed.; John Wiley & Sons, 2006.
(19) Sargent, E. H. Colloidal Quantum Dot Solar Cells. *Nat. Photonics* **2012**, *6*, 133−135.
(20) Livache, C.; Martinez, B.; Goubet, N.; Gréboval, C.; Qu, J.; Chu, A.; Royer, S.; Ithurria, S.; Silly, M. G.; Dubertret, B.; Lhuillier, E. A Colloidal Quantum Dot Infrared Photodetector and Its Use for Intraband Detection. *Nat. Commun.* **2019**, *10*, 2125.
(21) Moreels, I.; Lambert, K.; Smeets, D.; De Muynck, D.; Nollet, T.; Martins, J. C.; Vanhaecke, F.; Vantomme, A.; Delerue, C.; Allan, G.; Hens, Z. Size-Dependent Optical Properties of Colloidal PbS Quantum Dots. *ACS Nano* **2009**, *3*, 3023−3030.
(22) Brown, P. R.; Lunt, R. R.; Zhao, N.; Osedach, T. P.; Wanger, D. D.; Chang, L.-Y.; Bawendi, M. G.; Bulovic, V. Improved Current Extraction from ZnO/PbS Quantum Dot Heterojunction Photovoltaics Using a MoO3 Interfacial Layer. *Nano Lett.* **2011**, *11*, 2955−2961.
(23) Gao, J.; Perkins, C. L.; Luther, J. M.; Hanna, M. C.; Chen, H.-Y.; Semonin, O. E.; Nozik, A. J.; Ellingson, R. J.; Beard, M. C. n-Type Transition Metal Oxide as a Hole Extraction Layer in PbS Quantum Dot Solar Cells. *Nano Lett.* **2011**, *11*, 3263−3266.
(24) Talapin, D. V.; Lee, J.-S.; Kovalenko, M. V.; Shevchenko, E. V. Prospects of Colloidal Nanocrystals for Electronic and Optoelectronic Applications. *Chem. Rev.* **2010**, *110*, 389−458.
(25) Beek, W. J. E.; Wienk, M. M.; Kemerink, M.; Yang, X.; Janssen, R. A. J. Hybrid Zinc Oxide Conjugated Polymer Bulk Heterojunction Solar Cells. *J. Phys. Chem. B* **2005**, *109*, 9505−9516.
(26) Woo, H. K.; Kang, M. S.; Park, T.; Bang, J.; Jeon, S.; Lee, W. S.; Ahn, J.; Cho, G.; Ko, D.-K.; Kim, Y.; Ha, D.-H.; Oh, S. J. Colloidal-Annealing of ZnO Nanoparticles to Passivate Traps and Improve Charge Extraction in Colloidal Quantum Dot Solar Cells. *Nanoscale* **2019**, *11*, 17498−17505.
(27) Shi, G.; Wang, Y.; Liu, Z.; Han, L.; Liu, J.; Wang, Y.; Lu, K.; Chen, S.; Ling, X.; Li, Y.; Cheng, S.; Ma, W. Stable and Highly Effcient PbS Quantum Dot Tandem Solar Cells Employing a Rationally Designed Recombination Layer. *Adv. Energy Mater.* **2017**, *7*, 1602667.
(28) Martyniuk, P.; Rogalski, A. Quantum-Dot Infrared Photodetectors: Status and Outlook. *Prog. Quantum Electron.* **2008**, *32*, 89−120.
(29) Ye, Z.; Campbell, J. C.; Chen, Z.; Kim, E. T.; Madhukar, A. InAs Quantum Dot Infrared Photodetectors with $In_{0.15}Ga_{0.85}As$ Strain-Relief Cap Layers. *J. Appl. Phys.* **2002**, *92*, 7462−7468.
(30) Macabebe, E. Q. B.; van Dyk, E. E. Parameter Extraction from Dark Current-Voltage Characteristics of Solar Cells. *S. Afr. J. Sci.* **2008**, *104*, 401−404.
(31) Cheng, Y.; Whitaker, M. D. C.; Makkia, R.; Cocklin, S.; Whiteside, V. R.; Bumm, L. A.; Adcock-Smith, E.; Roberts, K. P.; Hari, P.; Sellers, I. R. Role of Defects and Surface States in the Carrier Transport and Nonlinearity of the Diode Characteristics in PbS/ZnO Quantum Dot Solar Cells. *ACS Appl. Mater. Interfaces* **2017**, *9*, 13269−13277.
(32) Shah, J. M.; Li, Y. L.; Gessmann, T.; Schubert, E. F. Experimental Analysis and Theoretical Model for Anomalously High Ideality Factors (n≫2.0) in AlGaN/GaN p−n Junction Diodes. *J. Appl. Phys.* **2003**, *94*, 2627−2630.
(33) Zhu, D.; Xu, J.; Noemaun, A. N.; Kim, J. K.; Schubert, E. F.; Crawford, M. H.; Koleske, D. D. The Origin of the High Diode-Ideality Factors in GaInN/GaN Multiple Muantum Well Light-Emitting Diodes. *Appl. Phys. Lett.* **2009**, *94*, 081113.
(34) Wenham, S. R.; Green, M. A.; Watt, M. E.; Corkish, R. *Applied Photovoltaics*, 2nd ed.; Routledge, 2006.
(35) Li, C.; Song, Z.; Zhao, D.; Xiao, C.; Subedi, B.; Shrestha, N.; Junda, M. M.; Wang, C.; Jiang, C.-S.; Al-Jassim, M.; Ellingson, R. J.; Podraza, N. J.; Zhu, K.; Yan, Y. Reducing Saturation-Current Density to Realize HighEffciency Low-Bandgap Mixed Tin−Lead Halide Perovskite Solar Cells. *Adv. Energy Mater.* **2019**, *9*, 1803135.
(36) Proctor, C. M.; Nguyen, T. Q. Effect of Leakage Current and Shunt Resistance on the Light Intensity Dependence of Organic Solar Cells. *Appl. Phys. Lett.* **2015**, *106*, 083301.
(37) Bederak, D.; Balazs, D. M.; Sukharevska, N. V.; Shulga, A. G.; Abdu-Aguye, M.; Dirin, D. N.; Kovalenko, M. V.; Loi, M. A. Comparing Halide Ligands in PbS Colloidal Quantum Dots for Field-

Effect Transistors and Solar Cells. *ACS Appl. Nano Mater.* **2018**, *1*, 6882−6889.
(38) Clark, P. C. J.; Neo, D.; Ahumada-Lazo, R.; Williamson, A. I.; Píš, I.; Nappini, S.; Watt, A. A. R.; Flavell, W. R. Influence of Multi-Step Surface Passivation on the Performance of PbS Colloidal Quantum Dot Solar Cells. *Langmuir* **2018**, *34*, 8887−8897.
(39) Nag, A.; Kovalenko, M. V.; Lee, J. S.; Liu, W.; Spokoyny, B.; Talapin, D. V. Metal-Free Inorganic Ligands for Colloidal Nanocrystals: S^{2-}, HS^{-}, Se^{2-}, HSe^{-}, Te^{2-}, HTe^{-}, TeS_3^{2-}, OH^{-}, and NH_2^{-} as Surface Ligands. *J. Am. Chem. Soc.* **2011**, *133*, 10612−10620.
(40) Kovalenko, M. V.; Scheele, M.; Talapin, D. V. Colloidal Nanocrystals with Molecular Metal Chalcogenide Surface Ligands,. *Science* **2009**, *324*, 1417−1420.
(41) Sahu, A.; Khare, A.; Deng, D.; Norris, D. J. Quantum Confinement in Silver Selenide Semiconductor Nanocrystals. *Chem. Commun.* **2012**, *48*, 5458−5460.
(42) Hines, M. A.; Scholes, G. D. Colloidal PbS Nanocrystals with Size-Tunable Near-Infrared Emission: Observation of Post-Synthesis Self-Narrowing of the Particle Size Distribution. *Adv. Mater.* **2003**, *15*, 1844−1849.
(43) Zhang, J.; Crisp, R. W.; Gao, J.; Kroupa, D. M.; Beard, M. C.; Luther, J. M. Synthetic Conditions for High-Accuracy Size Control of PbS Quantum Dots. *J. Phys. Chem. Lett.* **2015**, *6*, 1830−1833.

https://doi.org/10.1021/acsami.1c14749
ACS Appl. Mater. Interfaces 2021, 13, 49043−49049